



CHALMERS
UNIVERSITY OF TECHNOLOGY

Highly Efficient Platinum-Free Photocatalytic Hydrogen Evolution From Low-cost Conjugated Polymer Nanoparticles

Downloaded from: <https://research.chalmers.se>, 2026-04-14 12:54 UTC

Citation for the original published paper (version of record):

Holmes, A., Pan, J., Wang, L. et al (2025). Highly Efficient Platinum-Free Photocatalytic Hydrogen Evolution From Low-cost Conjugated Polymer Nanoparticles. *Advanced Materials*, 37(40). <http://dx.doi.org/10.1002/adma.202507702>

N.B. When citing this work, cite the original published paper.

Highly Efficient Platinum-Free Photocatalytic Hydrogen Evolution From Low-cost Conjugated Polymer Nanoparticles

Alexandre Holmes, Jingwen Pan, Li Wang, Leandro Franco, Rafael R. Bicudo, Bo Albinsson, C. Moyses Araujo, Weiguo Zhu, Dongbo Wang, Thuc-Quyen Nguyen, Jiefang Zhu,* and Ergang Wang*

While the interest in hydrogen photocatalysis from organic semiconductors is rapidly growing, there is a necessity to achieve hydrogen production without platinum (Pt), considering its price, availability and toxicity. In this work, this is demonstrated that high hydrogen evolution reaction (HER) efficiencies can be achieved without the use of Pt. A series of low-cost conjugated polymers are designed around the dibenzothiophene-S,S-sulfoxide (BTSO) unit, and self-assembled as nanoparticles in water via the nanoprecipitation technique. This is highlighted that how side chain engineering, nanoparticle morphology and pH influence the hydrogen evolution rate. Optoelectronic properties are improved through a Donor-Acceptor structure, resulting in an unprecedented hydrogen evolution reaction rate of 209 mmol g⁻¹ h⁻¹ in the absence of Pt. A clear correlation between high efficiencies and number of BTSO units within the polymer backbone can be established. The design rules pioneer the design of future organic materials is presented for a cost-efficient and sustainable hydrogen photocatalysis.

energies such as tidal, solar and wind are limited by their intermittent nature, requiring a direct integration in electric grids or storage in batteries. However, it is necessary to find sustainable ways to store this energy, if possible in the form of green fuels. In this context, hydrogen gas (H₂) is an excellent candidate, only producing water as a side product of its combustion or use in fuel cells.^[1] Photocatalysis (PC) enables the direct conversion of solar energy into chemical bonds such as in the form H₂, and is therefore regarded as a promising alternative solution for energy conversion and storage.^[2] The work of Pin-aud et al. pioneered the concept that aqueous dispersions would be the most cost-efficient approach for photocatalysis at a large scale.^[3] Through this nanoparticulate approach, the specific surface of the

photocatalysts can be significantly increased, promoting exchanges with the aqueous media.

Previous studies focused on inorganic photocatalysts but suffered from low conversion efficiencies due to an

1. Introduction

A shift from fossil fuels to carbon-neutral energy sources is more than ever necessary to fight against climate change. Renewable

A. Holmes, L. Wang, L. Franco, B. Albinsson, E. Wang
 Department of Chemistry and Chemical Engineering
 Chalmers University of Technology
 Göteborg SE-412 96, Sweden
 E-mail: ergang@chalmers.se

J. Pan, J. Zhu
 Department of Chemistry – Ångström
 Ångström laboratory
 Uppsala University
 Uppsala SE-75121, Sweden
 E-mail: jiefang.zhu@kemi.uu.se

J. Pan, D. Wang
 School of Materials Science and Engineering
 Harbin Institute of Technology
 Harbin 150001, China

L. Wang, W. Zhu
 School of Materials Science and Engineering
 Jiangsu Key Laboratory of Environmentally Friendly Polymeric Materials
 Jiangsu Collaborative Innovation Centre of Photovoltaic Science and
 Engineering
 Changzhou University
 Changzhou 213164, China

L. Franco, R. R. Bicudo, C. M. Araujo
 Department of Engineering and Physics
 Karlstad University
 Karlstad 65188, Sweden

R. R. Bicudo
 Institute of Physics
 University of São Paulo
 Rua do Matão 1371 CP 66318, São Paulo, SP CEP 05508-090, Brazil

R. R. Bicudo, C. M. Araujo
 Materials Theory Division
 Department of Physics and Astronomy
 Uppsala University
 Uppsala 75120, Sweden

T.-Q. Nguyen
 Center for Polymers and Organic Solids
 University of California
 Santa Barbara, CA 93106, USA

The ORCID identification number(s) for the author(s) of this article can be found under <https://doi.org/10.1002/adma.202507702>

© 2025 The Author(s). Advanced Materials published by Wiley-VCH GmbH. This is an open access article under the terms of the [Creative Commons Attribution-NonCommercial](https://creativecommons.org/licenses/by-nc/4.0/) License, which permits use, distribution and reproduction in any medium, provided the original work is properly cited and is not used for commercial purposes.

DOI: 10.1002/adma.202507702

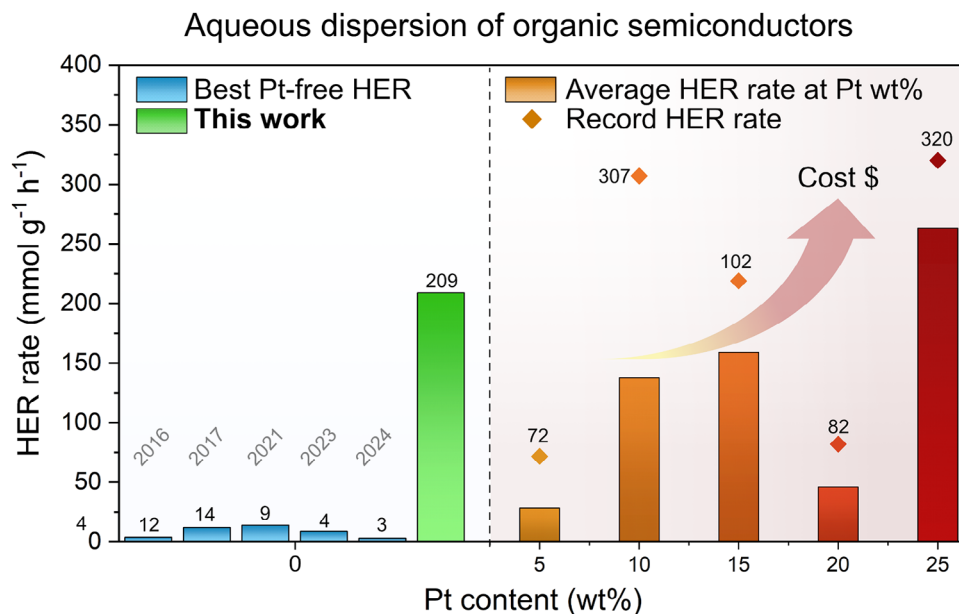


Figure 1. Reported Hydrogen Evolution Reaction (HER) rates in the literature, updated in January 2025, and compared to the HER rate achieved in this work. Pt-free reports are presented according to the record efficiencies over the last years. Pt-containing systems are presented according to Pt content in weight percent (wt%) relative to the photocatalyst mass. Both average and record HER rates were extracted from a representative panel of literature listed in the Table S1 (Supporting Information).

absorption range limited in the UV region. Organic semiconductors present the advantage of versatile photoelectronic properties, in which their absorption can be easily tuned through molecular engineering.^[4,5] Their wide absorption ranges from UV to the near infrared (IR), tailored energy levels, and improved processability make them excellent candidates for photocatalysis. Such a wide spectra of properties resulted in an exponential growth of interest for organic photocatalysts over the last 10 years.^[6]

A particular attention has been given to the dibenzothiophene-S,S-sulfoxide (BTSO) unit, and has led to the development of cost-efficient materials for photocatalysis.^[7-9] Hillman et al. highlighted that the high polarity of the sulfone group significantly enhances the overall water affinity of the photocatalyst, hence its photocatalytic activity.^[10] While the catalytic cycle of BTSO-based material might not be fully understood, Sachs et al. proposed that after photoexcitation, the exciton formed in BTSO-based materials is quenched through hole transfer to a sacrificial electron donor (SED), resulting the formation of in an electron polaron, further transferred to a cocatalyst.^[11] However, linear polymer designs (without side chains) are typically adopted, requiring a tedious processing through ultrasonication in mixed solvents (water and dimethylformamide, N-methyl-2-pyrrolidone or methanol) to achieve an organic dispersion.^[12-14] Several candidates achieved high hydrogen evolution reaction (HER) rates, superior to 100 mmol g⁻¹ h⁻¹, without the aid of Pt-cocatalyst, and offered excellent hints toward the direction to follow in terms of backbone design.^[12,15] However, efforts should be employed to overcome their poor processability and shift from toxic solvent mixtures to pure water media. For instance, by removing all toxic solvents from the aqueous media, a loss of the photocatalytic activity was reported, and was likely related to the lower accessibility

of proton to the reactive sites due to strong aggregation of polymer chains.^[16]

Post-synthesis techniques such as nanoprecipitation or miniemulsion allow the processing of conjugated materials as nanoparticles dispersed in water, with a high control toward the nanoparticle size.^[17] When confined at the nanoscale, improved photocatalytic properties could be achieved in comparison to large aggregates.^[18] Through optimization of the photocatalyst choice, nanoparticle morphology and dispersion stability, an exponential growth in efficiencies has been observed in the last 5 years.^[19-21] The combination of electron donor (D) and electron acceptor (A) materials within a single nanoparticle resulted in wider light absorption range and improved exciton dissociation efficiency, increasing the overall solar-to-hydrogen conversion yield,^[22,23] but are often associated to a high synthetic complexity, difficult nanoparticle preparation and lower stability.

However, it is important to point out that most of the reports using aqueous dispersions of organic semiconductors rely on the addition of expensive cocatalysts, such as platinum (Pt) (Figure 1; Table S1, Supporting Information).^[24-26] When scrutinizing the literature, the focus on reaching high efficiencies (>50 mmol g⁻¹ h⁻¹) led to a systematic photodeposition of Pt onto the nanoparticle surface, and a material design centred on wide light absorption range and improved charge transfer to Pt cocatalysts.^[27] While alternative co-catalysts were investigated in the literature, the focus was mostly on inorganic photocatalyst systems, with additional steps required to yield encouraging efficiencies.^[28,29] When considering Pt-free photocatalysts reported in literature, only a few systems have been investigated and modest efficiencies have been reported, with a HER rate of 14 mmol g⁻¹ h⁻¹.^[18,30-34] Therefore, it is necessary to demonstrate

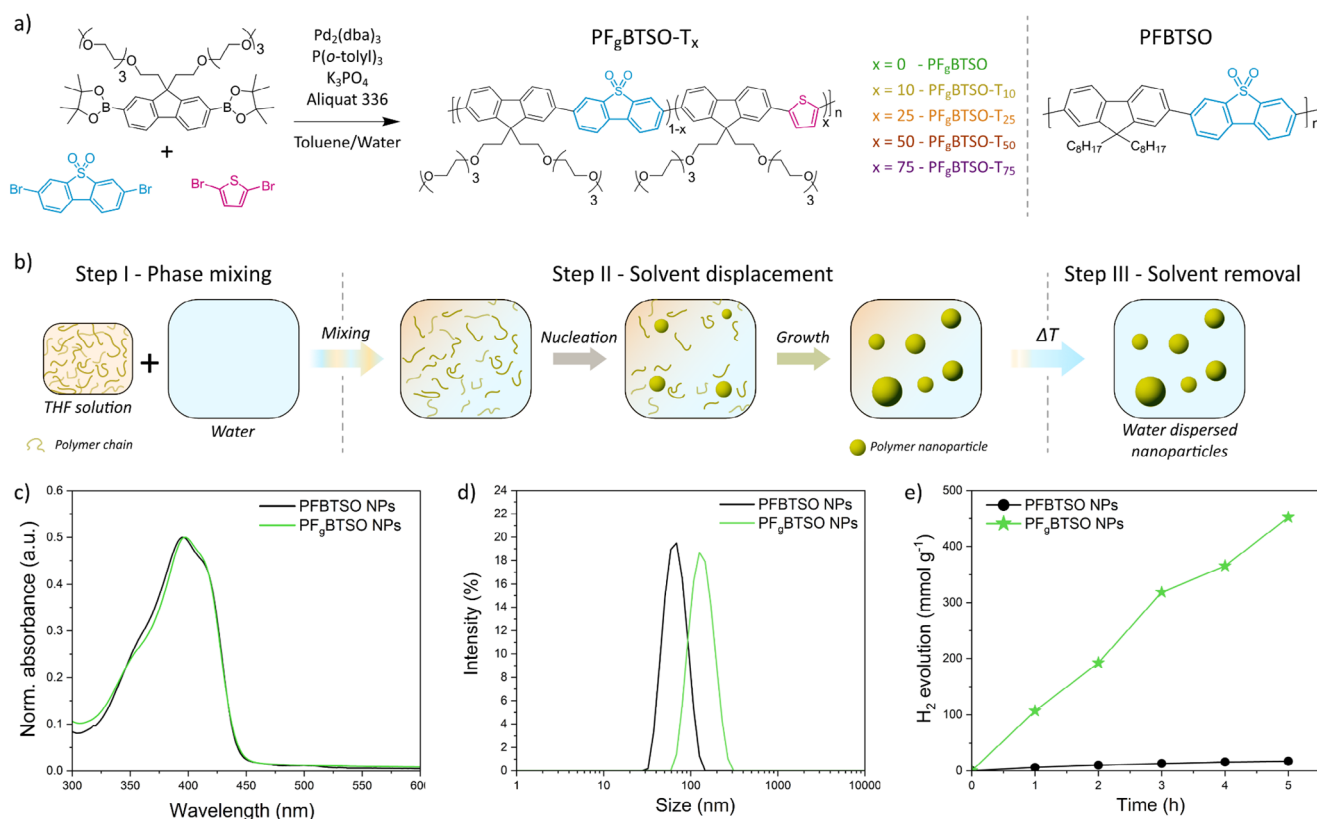


Figure 2. a) Chemical structure of the polymers synthesized through a Suzuki-Miyaura cross-coupling polycondensation, highlighting in blue the electron accepting BTSO unit and in pink the electron donating thiophene unit. b) Schematic representation of the nanoprecipitation mechanism, resulting in water-dispersed nanoparticles. c) Absorption, d) nanoparticle size distribution and e) hydrogen evolution of PFBTSO and PF_gBTSO nanoparticles dispersed in water. Absorption spectra intensities were normalised at 405 nm. Photocatalytic experiments were performed using 0.25 mg of polymer nanoparticles in 10 mL of water, 0.1 M of ascorbic acid, no additional Pt cocatalyst and under 1 sun.

that high efficiencies for hydrogen photocatalysis can be achieved with Pt-free materials, especially when considering the high cost, limited availability and potential toxicity of Pt.^[35]

In this work, we highlight that nanoparticles comprising a conjugated polymer without addition of Pt can deliver a high HER rate, comparable to other organic photocatalysts with expensive Pt. We combined an efficient material design based on the BTSO unit with an optimized nanoprecipitation technique to achieve highly efficient and stable water dispersions for photocatalytic hydrogen production. The introduction of polar oligo-ethylene glycol (OEG) side chains was key to significantly improve the photocatalytic efficiencies. Through experimental and theoretical investigations, we highlighted that a more hydrated structure was achieved in presence of OEG side chains, allowing a better accessibility to the sulfone units for the protons and ascorbic acid. The design of a donor-acceptor-like molecular structure through the introduction of thiophene units resulted in enhanced optoelectronic properties alongside a better understanding of the crucial role of BTSO units. We demonstrated that final efficiencies relied on a delicate balance between improved absorption range, charge generation, stability, and number of BTSO units. In addition, we highlighted the crucial impact of pH value toward photocatalytic efficiencies. In optimized conditions, we reported an outstanding HER rate of 209 mmol g⁻¹ h⁻¹ in absence of any Pt cocata-

lyst, paving the way for the future of a more sustainable hydrogen photocatalysis.

2. Results

2.1. Polymer Synthesis and Preparation of Dispersion

A series of polymers based on the BTSO accepting unit were synthesized, with two low-cost and widely accessible units: fluorene linkers and thiophene (T) donating units (**Figure 2a**). Two polymers based on BTSO and fluorene units, either alkylated (PFBTSO) or glycolated (PF_gBTSO), were synthesized to understand the impact of the side chains toward hydrogen photocatalysis. Then, a range of polymers presenting a donor-acceptor structure and polar side chains were synthesized. The content of thiophene units within the polymer backbone is directly represented in their name (i.e., PF_gBTSO-T₁₀ for 10% of substitution). The final ratio between BTSO and T units in terpolymers was attested by ¹H NMR (Figures S1–S7, Supporting Information). These results are in close agreement with the targeted ratios, and the ratios initially targeted are used for nomenclature of the designed polymers.

The resulting polymers presented a low cost (<\$20 g⁻¹, Table S2, Supporting Information), and were obtained through

simple synthetic procedures, making them suited candidates for upscaling.^[36] In comparison, organic semiconductors used in the field of photocatalysis, such as low band gap conjugated polymers and non-fullerene acceptors (i.e., PM6 and Y6), usually present a high cost (>\$150 g⁻¹) and complex synthetic procedures.^[37] Although the BTSO unit is simple and low-cost, the selection of comonomer is also the key to bring down the cost of the resulting polymers, and should be considered for future designs.

In addition, all polymers presented comparable molar masses ($M_n \approx 15 \text{ kg mol}^{-1}$) according to SEC measurements calibrated against polystyrene (Figure S8, Supporting Information). Their energy levels were calculated through cyclic voltammetry measurements, and displayed enough driving force, in theory, to ensure photocatalytic proton reduction and ascorbic acid (AA) oxidation (Figures S9 and S10, Supporting Information). Finally, as photocatalytic reactions are occurring in water, their hydrophilicity was investigated through surface energy calculations. A significant increase from 26.5 mN m^{-1} in the case of PFBTSO to over 35 mN m^{-1} for all derivatives bearing ethylene glycol side chains was observed, attesting a more hydrophilic behavior (Figure S11 and Table S3, Supporting Information).

Several preparations can be employed to achieve aqueous dispersions of organic semiconductors, but the miniemulsion and the nanoprecipitation techniques are the most represented.^[22] Other processing methods can be considered for the preparation of polymer nanoparticles. For example, polymerization in emulsion offers a direct synthesis of polymer nanoparticles, but extra steps of purification might be required to remove side-products.^[38,39] Electrospinning can also be considered for the design of controlled nanofibers with defined sizes, but additional steps are required to achieve water-processed materials.^[40,41]

We decided to focus on the nanoprecipitation technique (Figure 2b), owing to its simple principle,^[17] excellent reproducibility and scalability through continuous flow synthesis.^[42–44] After solubilization of the conjugated polymers in tetrahydrofuran (THF) (Step I), a small volume of organic solution is poured in a larger volume of water under strong stirring.^[45] Due to the miscibility of THF and water, the mixture quickly becomes an insoluble media for the polymer chains (Step II). A first mechanism of nucleation results in the aggregation of polymer chains as nuclei, quickly followed by a growth mechanism inducing the accumulation of remaining polymer chains on the nearest nuclei. As a result, nanoparticles are formed in a very short timescale, prior the removal of THF. The last step is the removal of THF to obtain water dispersions (Step III). Once prepared the dispersions showed a high stability and could be stored in the dark for several months (Figure S12, Supporting Information).

2.2. Impact of Side Chains Toward Hydrogen Evolution Reaction

The alkylated and glycolated polymers, PFBTSO and PF_gBTSO respectively, were compared to understand the role of the side chains toward nanoparticle formation, properties and impact on photocatalytic hydrogen evolution. Both dispersions displayed an absorption profile in the UV-visible region (Figure 2c), slightly redshifted in comparison to their chloroform solution, and close to the profile obtained from thin films (Figure S13, Supporting

Information), indicating the existence of interchain aggregation within the nanoparticles.

For clarity, nanoparticle sizes discussed along the manuscript corresponds to the average hydrodynamic diameter obtained from dynamic light scattering (DLS) measurements. Stable dispersions with nanoparticle size of 80 and 130 nm were achieved for PFBTSO and PF_gBTSO, respectively (Figure 2d). The larger size distribution observed for PF_gBTSO could be attributed to a more hydrated structure, while the strong hydrophobicity of PFBTSO will limit the interactions with the aqueous media. Photocatalytic experiments were performed by addition of AA as sacrificial donor (0.1 M), illumination under a light intensity of 1 sun, and no additional Pt cocatalyst. A HER rate of $90 \text{ mmol g}^{-1} \text{ h}^{-1}$ was achieved for PF_gBTSO nanoparticles after 5 h, while PFBTSO nanoparticles only achieved a rate of $3 \text{ mmol g}^{-1} \text{ h}^{-1}$ (Figure 2e). To understand the origin of such enhancement, we investigated the impact of side chains toward the redox properties of PFBTSO and PF_gBTSO, and on the polymer aggregation within the nanoparticle.

No considerable changes in the electron density distribution over the polymers' backbone were promoted by the shift from alkyl to OEG side chains, as indicated by the projected density of states and electrostatic potential calculations (Figures S14 and S15, Supporting Information). However, the overall molecular polarity of the polymer, in both the ground and first excited states, increased by $\approx 30\%$ due to the presence of OEG side chains. Additionally, the calculated redox potential of PF_gBTSO displayed slightly higher driving forces for proton reduction and AA oxidation in comparison to PFBTSO (Figure S16 and Tables S4 and S5, Supporting Information). For more details regarding the two-hole oxidation of AA to dehydroascorbic acid (DHA), refer to the Note S1 (Supporting Information).^[46] However, the drastic difference in HER rates observed experimentally is unlikely related only to a slight change in redox potentials.

Molecular Dynamics (MD) simulations were performed to investigate the impact of side chains on nanoparticle formation (Figure 3a,b; Figure S17, Supporting Information). A closely packed structure was achieved for PFBTSO, similar to lipid tails in biological systems,^[47] likely due to the high hydrophobicity of alkylated side chains. Hydration of polymer chains is enhanced in the presence of glycol side chains for PF_gBTSO nanoparticles, evidenced by the radial distribution function of water molecules around the sulfone groups (Figure S18, Supporting Information). In addition, the nanoparticle size of the simulated nanoparticles was larger for PF_gBTSO nanoparticles ($\approx 5.1 \text{ nm}$) when compared to PFBTSO nanoparticles ($\approx 2.5 \text{ nm}$), while keeping constant the number of polymer chains assembled as nanoparticles. Taken together, these calculations indicate that a more hydrated structure should be achieved for PF_gBTSO nanoparticles, in agreement with its higher surface energy and the larger nanoparticle size experimentally probed.

To further investigate the interaction of the polymer chains with AA during the hole transfer process, additional MD simulations were performed using a simplified polymer model. In comparison to PFBTSO, PF_gBTSO allowed a better permeation of ionic species closer to the polymer backbone (Figure S19, Supporting Information). In addition, as observed by Hu et al., the presence of glycol side chains appeared to result in beneficial interactions with protons (Figure S20, Supporting Information).^[48]

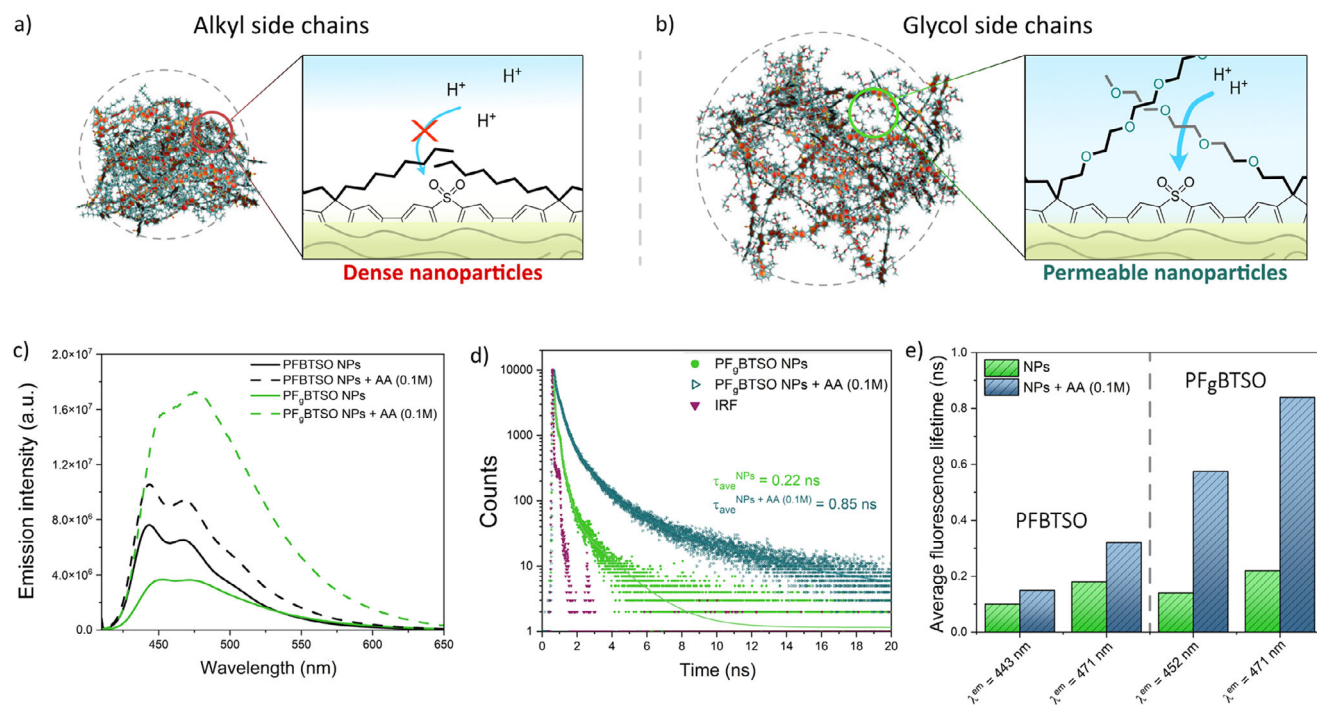


Figure 3. MD configurations of a) PFBTSO and b) PF_gBTSO NPs simulated in water, with schematic representation of the accessibility to the polymer backbone and sulfone units for protons solvated in water, depending on the side chain and nanoparticle morphology. The calculated nanoparticle size of each nanoparticle is represented with the dashed circle, highlighting the formation of larger nanoparticles for PF_gBTSO. c) Emission spectra of PFBTSO and PF_gBTSO NPs with and without the addition of AA (0.1 M). Excitation wavelength of 405 nm. d) Fluorescence decay dynamics of PF_gBTSO NPs with and without the addition of AA (0.1 M), probed on the main component at 471 nm, with fitting of the decay in solid lines and instrument response function plots. e) Evolution of fluorescence average lifetimes upon addition of AA (0.1 M) for both PFBTSO and PF_gBTSO nanoparticles, considering the two main components observed in the fluorescence profile.

Put all together, these results indicate a more favourable interaction between protons and AA with the polar polymers.

To experimentally probe the interactions of AA with the polymer backbone, steady state and time-resolved photoluminescence measurements were performed. Prior to the addition of AA, a lower fluorescence yield can be observed for PF_gBTSO nanoparticles in comparison to PFBTSO nanoparticles, and might be attributed to a higher permittivity and dipole moment brought from the polar side chains.^[49,50] Through the addition of AA (0.1 M), an enhancement of fluorescence intensity for both polymers was observed (Figure 3c), more pronounced for PF_gBTSO nanoparticles. This observation is also consistent with their extended excited state lifetimes (Figure 3d,e; Figure S21 and Table S6, Supporting Information). Such increase in fluorescence intensity and lifetime could be the result of a change of the nanoparticle morphology or the reduction of charge transfer properties, and the next section is dedicated to understand which is the most likely.^[51,52] The nanoparticle morphology is defined as the aggregation of polymer chains within the nanoparticle, hence comprising the nanoparticle porosity.

Upon the addition of AA, an increase of nanoparticle size was identified, while no changes were observed on the absorption profile (Figures S22 and S23, Supporting Information). The increased nanoparticle size appears well correlated with the increased emission of PF_gBTSO nanoparticles. Owing to the high interactions between AA and the OEG side chains, a swelling due to the presence of AA or H⁺ species within the nanoparticle

would explain the increased nanoparticle size. As the nanoparticle swells, the aggregation of polymer chains shifts toward an H-type aggregation that could explain the increased and red-shifted emission, the decrease of 0-0 to 0-1 vibronic peak ratio alongside the formation of longer-lived excited states.^[53] According to our previous MD simulations, a denser morphology would be achieved in the case of PFBTSO, which explains the lower impact of addition of AA onto the nanoparticle morphology and emission properties. Furthermore, the addition of AA could result in a change of torsional angles between the fluorene and BTSO units, reduced from 33.4° to 18.0° and from 34.2° to 15.4° for PFBTSO and PF_gBTSO, respectively, for the optimized geometries with AA as a solvent (see Note S2, Supporting Information). Therefore, an increase of planarity upon the addition of AA could result in an alteration of the nanoparticle morphology, also resulting in enhanced emissions.

In a second time, we investigated if the enhancement in emission intensity could arise from a charge transfer. We measured the evolution of fluorescence by replacing AA with triethylamine (TEA, another commonly used sacrificial donor) or HCl, both at a concentration of 0.1 M. The same enhancement of fluorescence has been observed, indicating that such behaviour is not related to a charge transfer process, as no charge transfer pathways are promoted with the addition of HCl (Figure S24, Supporting Information). Additional photoluminescence experiments in chloroform solution were performed to investigate the impact of sacrificial agents when both polymers are readily soluble. Due to the

insolubility of AA in chloroform, TEA was selected to investigate the emission changes of PFBTSO and PF_gBTSO. A quenching of fluorescence was achieved in presence of TEA for both solubilised polymers, regardless of the side chains, indicating charge transfer between the polymer and SED (Figure S25, Supporting Information). Therefore, the idea that the addition of AA would increase the PL intensity due to a charge transfer is not supported.

Such observations confirmed that the origin of the enhanced emission when using aqueous dispersions might come from a change in nanoparticle morphology and not be related to charge transfers. Only few works investigated the impact of the addition of AA, with only a slight quenching observed.^[54] In their case, highly hydrophobic and dense nanoparticles were achieved, which might limit the impact of AA onto the nanoparticle morphology, and only charge transfer would occur, resulting in slightly quenched fluorescence. Therefore, we hypothesize that the introduction of ionic species promotes a swelling of the nanoparticle, as an increased nanoparticle size was identified by DLS measurements. This swelling alters the nanoparticle morphology, with a shift toward H-type aggregation, leading to the formation of long-lived excited states offering more time for electron transfer to H⁺ or hole transfer to the sacrificial donor, which is beneficial for enhancing HER. Furthermore, a better accessibility of the reactive sites is achieved due to a nanoparticle swelling and could also benefit hydrogen evolution. Finally, the presence of AA should also allow for charge transfer to occur, resulting a quenching of the emission. However, the competition between fluorescence quenching due to charge transfer and fluorescence enhancement due to nanoparticle swelling appears to be more favourable for the latter. To the best of our knowledge, this is the first report of enhanced emission from conjugated nanoparticles in presence of ionic species in a water dispersion.

Several works highlighted the importance of side chains engineering, with enhanced efficiencies achieved using OEG side chains, due to a higher dipole moment, reduced recombination and improved water affinity.^[49,55] However strongly aggregated materials were usually reported, leaving no room for the OEG side chains to influence the nanoparticle formation. Therefore, we investigated the importance of the preparation technique toward the nanoparticle morphology. The nanoprecipitation allows for the formation of nanoparticles through the diffusion a THF solution (containing the polymer chains) and water. The resulting morphology dependent from the hydrophilicity of the polymer: dense structures for hydrophobic polymers, more porous and water permeable in the case of hydrophilic polymers. Therefore, two additional techniques with different nanoparticle formation mechanisms were investigated, in theory not allowing the formation of permeable structures.

PF_gBTSO dispersions were prepared using the ultrasonication approach, according to reported literature (Figures S26 and S27, Supporting Information).^[55] In the best conditions, a HER rate of 2.3 mmol g⁻¹ h⁻¹ was achieved (similar to the HER rates achieved by Woods et al.),^[55] 30 times lower than that achieved from PF_gBTSO nanoparticles prepared through the nanoprecipitation (90 mmol g⁻¹ h⁻¹). We hypothesize that the large aggregate size (≈2 μm) and denser structure are the reason behind such decreased efficiencies, further highlighting the importance of processing.

Then, PF_gBTSO nanoparticles were prepared through the miniemulsion.^[49] In this case, the polymers are initially solubilized in chloroform droplets and stabilized by surfactant molecules. During the evaporation of the organic solvent, the polymer chains aggregate as nanoparticles without strong exchanges with the aqueous media, ultimately confined by the surfactant molecules. Upon photocatalysis, a HER rate of 1.3 mmol g⁻¹ h⁻¹ was achieved (Figure S28, Supporting Information), lower than that from PF_gBTSO nanoparticles prepared through the nanoprecipitation. Despite the smaller nanoparticles achieved (83 nm for miniemulsion against 130 nm for the nanoprecipitation), the formation of dense nanoparticles, alongside the presence of surfactant at the nanoparticle surface, might be the reasons behind the lower efficiencies.

To summarize, the primary reasons for the high HER rates observed in presence of OEG side chains appeared to be linked to the nanoparticle morphology and the preparation technique. When combining polar side chains and the nanoprecipitation technique, more hydrated structures were achieved, which significantly improve the accessibility to the reactive sites. In addition, OEG side chains promoted the interactions with AA and H₃O⁺ ions with the polymer backbone, beneficial to achieve efficient hydrogen photocatalysis. Finally, the change in nanoparticle aggregation upon addition of ionic species, such as AA, resulted in enhanced fluorescence intensity and excited-state lifetimes. Taken all together, all these improvements promote hydrogen photocatalysis, and are the reason behind the superior photocatalytic activity of PF_gBTSO in comparison to PFBTSO.

2.3. Toward Record HER Rates Through Backbone Engineering

In order to improve the optoelectronic properties of BTISO-based polymers, a donor-acceptor structure was designed, where BTISO units were partially substituted by thiophene units (PF_gBTISO-T_x), with a gradient from 10 to 75% of substitution. The addition of thiophene units resulted in a decrease of the bandgap mostly through increase of HOMO levels, thus not affecting the driving forces of proton reduction. Such D-A structure is expected to improve charge delocalization with a higher electron density within the sulfone group.^[56]

Upon nanoprecipitation, stable dispersions with sizes ranging from 60 to 120 nm were achieved (Figure S29 and Table S7, Supporting Information). Introduction of thiophene resulted in a redshift in absorption maxima from 400 to 440 nm (Figure 4a), with the growth of a shouldering ≈458 nm, linked to stronger π-π interactions. A more pronounced change in the electronic properties can be observed in fluorescence, with quenched and redshifted emission spectra (Figure 4b), alongside the formation of longer-lived excited states (Figure S30, Supporting Information). The addition of AA significantly enhanced the emission yields and excited state lifetime (≈1 ns) for all PF_gBTISO-T_x derivatives (Table S8, Supporting Information). Upon photocatalysis, the beneficial impact of thiophene substitution resulted in HER rates up to 162 mmol g⁻¹ h⁻¹ for PF_gBTISO-T₂₅ (Figure 4c; Figure S31, Supporting Information). However, a quick drop in efficiency was observed at higher thiophene content, regardless of the improved excited state lifetime and absorption range, with only 13 mmol g⁻¹ h⁻¹ achieved by PF_gBTISO-T₇₅. To ensure that such lower

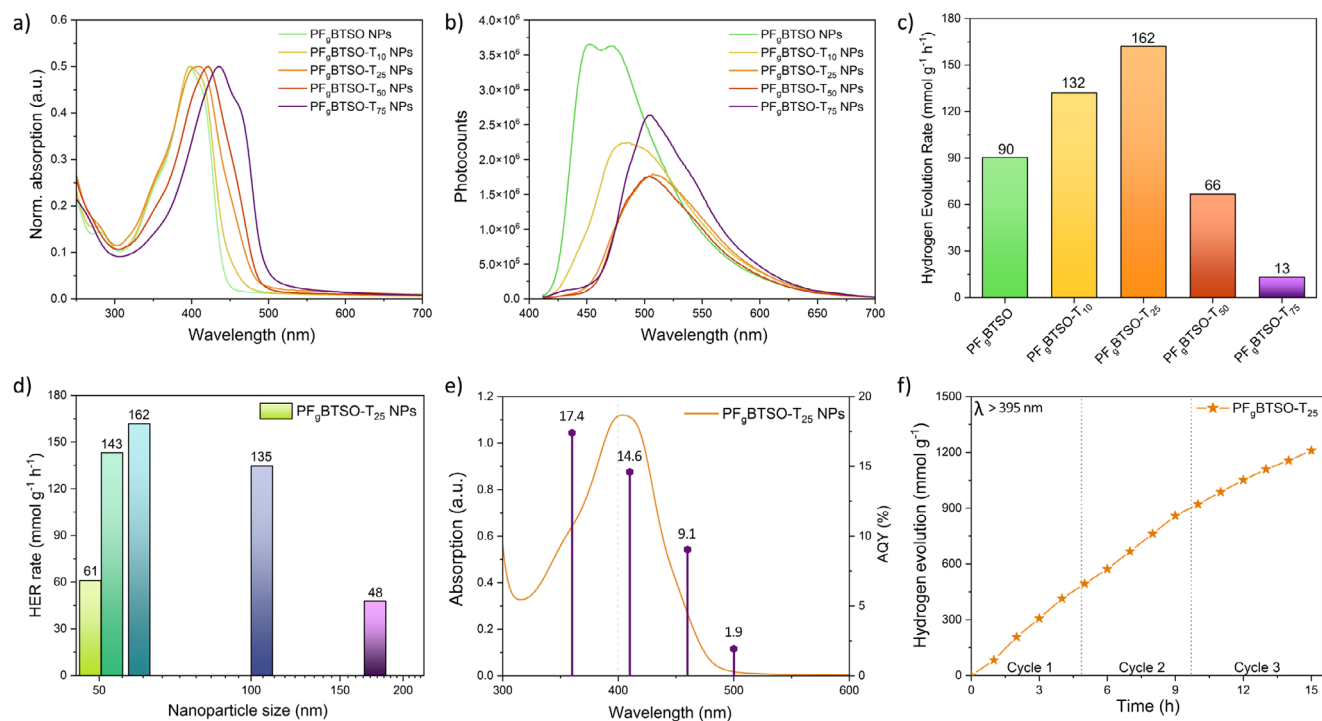


Figure 4. a) Absorption and b) emission spectra of $\text{PF}_6\text{BTSO-T}_x$ dispersions in water with different thiophene content. Absorption spectra intensities were normalized at the maximum wavelength for each dispersion. An excitation wavelength of 405 nm was used for emission spectra. c) HER rates calculated after 5 h of photocatalysis for $\text{PF}_6\text{BTSO-T}_x$ water dispersions (0.1 M of AA and no additional Pt). d) HER rates calculated after 5 h of photocatalysis for $\text{PF}_6\text{BTSO-T}_{25}$ dispersions with various nanoparticle sizes (0.1 M of AA and no additional Pt). e) AQY of $\text{PF}_6\text{BTSO-T}_{25}$ dispersion in optimized conditions at wavelengths of 360, 410, 460 and 500 nm and corresponding UV-visible spectrum. f) Visible-light hydrogen evolution of $\text{PF}_6\text{BTSO-T}_{25}$ using a UV cutoff filter (>395 nm, 0.1 M of AA and no additional Pt). After each cycle, the concentration of AA was raised back to 0.1 M.

efficiencies are not linked to the nanoparticle size, $\text{PF}_6\text{BTSO-T}_{75}$ with nanoparticle sizes ≈ 68 nm were prepared (Figure S32 and Table S7, Supporting Information), but still yielded modest HER rates (21 $\text{mmol g}^{-1} \text{h}^{-1}$).

We further investigated the influence of the nanoparticle size toward photocatalytic hydrogen evolution. Dispersions of $\text{PF}_6\text{BTSO-T}_{25}$ were prepared with sizes ranging from 48 to 176 nm (Figure S33 and Table S7, Supporting Information) through change in the initial concentration of polymer in the THF solution. Despite a change in nanoparticle size, all dispersions showed similar absorption and emission profiles (Figures S34 and S35, Supporting Information). However, upon photocatalysis optimum efficiencies were achieved for sizes comprised between 53 and 105 nm (Figure 4d), showing an average HER rate ≈ 147 $\text{mmol g}^{-1} \text{h}^{-1}$. However, both extreme sizes synthesized (smallest and largest) displayed lower HER rates, linked to a clear loss of photocatalytic properties over time and visible material aggregation upon photocatalysis (Figure S36, Supporting Information). Nevertheless, the small variations in HER rates observed for nanoparticle size ranging from 53 to 105 nm indicate that the main impact of the nanoparticle size lies within the stability of the dispersion upon photocatalytic experiment.

Apparent quantum yield (AQY) measurements were performed to investigate which region of the light spectra was mostly involved in the photocatalytic conversion. While the absorption maximum is reached at 403 nm for $\text{PF}_6\text{BTSO-T}_{25}$, it appeared that a highest AQY of 17.4% was obtained at 360 nm, followed

by an AQY of 14% at 410 nm (Figure 4f; Figure S37, Supporting Information). Probing at higher wavelengths highlighted a photocatalytic behaviour up to 500 nm, with an AQY of 1.9%. While good AQYs are achieved in the visible range, it is necessary to avoid absorption in the UV-range, as high energy photons are known to degrade photocatalysts after long-time measurements (Figure S38, Supporting Information). Further work should focus on redshifting BTSO-based materials to enhance absorption in the visible range, thereby limiting degradation rate. Photocatalytic experiments over 15 h using a UV-cutoff filter (395 nm) revealed that $\text{PF}_6\text{BTSO-T}_{25}$ dispersions have a good stability when irradiated under visible light (Figure 4e), further proven with more than 32 h of stability when using a LED lamp (Figure S39, Supporting Information).

We further investigated the impact of pH toward photocatalytic activity. Such parameter is usually overlooked in the literature, either not reported or fixed at a pH value of 4, yet it can be decisive to optimize the HER rate.^[23,57–59] The two-hole oxidation pathways of AA requires the availability of the deprotonated intermediate (HA^-), which is limited by the equilibrium ($\text{H}_2\text{A} / \text{HA}^-$), where H_2A stands for the fully protonated AA. With a pKa of 4.04, it is expected that at a pH value of 4 the equilibrium is pushed at 50% toward the HA^- species (Figure S40, Supporting Information). In opposition, at a pH value of 2, a higher concentration of protons (0.01 M) will be available while only 1% of the ascorbic acid will be in the deprotonated HA^- form. At pH values of 2 and 4, HER rates of 118 and 98 $\text{mmol g}^{-1} \text{h}^{-1}$ were achieved,

respectively. The best HER rates were achieved at a pH value of 2.5 (183 mmol g⁻¹ h⁻¹) and 3 (168 mmol g⁻¹ h⁻¹), where only 3% and 10% of ascorbic acid was in the deprotonated form, respectively (Figure S31, Supporting Information). By reducing the pH values from 4 to 2, the concentration of H⁺ increases by 100-folds, but the lower availability of the HA⁻ species might result in accumulations of holes, with a bottleneck toward the hole transfer. On the other hand, a too high pH would limit the presence of H⁺, resulting in an accumulation of electrons within the polymer nanoparticles. As BTSO-based materials are known to show ultrafast hole transfer,¹⁰ we propose that a balance between available protons H⁺ (promoted at low pH) and HA⁻ species (promoted at neutral pH) must be achieved.

Finally, we investigated the impact of the photocatalyst concentration toward the HER rate. Nanoparticle concentrations from 8 to 50 μg mL⁻¹ were compared, but the best compromise in terms of HER rate and stability was achieved at a concentration of 25 μg mL⁻¹, yielding a HER rate of 183 mmol g⁻¹ h⁻¹, and 137 μmol h⁻¹ without normalization by photocatalyst mass (Figure S41, Supporting Information). The robustness of the approach was confirmed by performing HER experiments in two different research groups, with a good reproducibility, and slightly improved performances (10%) when using a top irradiation for photocatalytic experiments (Figure S42, Supporting Information). An excellent batch-to-batch reproducibility, with less than 3% of variability, could be achieved for PF_gBT_{SO}-T₂₅ nanoparticles (Figures S43, Supporting Information). The nanoprecipitation is therefore a suitable technique to achieve efficient and reproducible results for photocatalytic applications. In optimized conditions (top-irradiation, pH 2.5, Figure S44, Supporting Information), the final efficiencies could be improved to 209 mmol g⁻¹ h⁻¹.

2.4. The Origin of the High HER From the Pt-free Photocatalysts

Such HER rates are unusually high for conjugated polymer nanoparticles in absence of additional Pt cocatalyst, therefore, it is important to investigate their origin. Upon absorption of an incident photon, an exciton is generated within the polymer nanoparticles. This exciton can be further quenched, either through hole transfer to the SED or through electron transfer to protons. Previous investigations propose that an ultrafast hole transfer from the BT_{SO} unit to the SED happens after photoexcitation, resulting in the generation of an electron polaron. The latter is then transfer to the cocatalyst sites at a slow rate, making this kinetic the bottle-neck of hydrogen generation.¹⁰ In most cases, the cocatalyst was identified as residual Pd from the synthesis of the conjugated polymers. However, when scrutinizing the literature, various content of Pd were reported for BT_{SO}-containing polymers (<100 to >20 000 ppm) and displayed similar HER (<5 mmol g⁻¹ h⁻¹).^[7,31,55,60,61] Therefore, it is doubtful to attribute solely the hydrogen evolution mechanism to a charge transfer to Pd, and another mechanism with the BT_{SO} unit as active site for HER should be considered, independent of the presence of the cocatalyst. Especially when considering that the HER performance achieved with PF_gBT_{SO}-T₂₅ NPs is far beyond those that have been previously reported.

To understand the impact of Pd, we first performed photocatalytic experiments on PF_gBT_{SO}-T₂₅ dispersion comprising dif-

ferent loading of residual Pd (measured by inductively coupled plasma mass spectrometry, ICP-MS, Table S9, Supporting Information) (Figure 5a). The change of Pd content did not affect the final HER rates (≈183 mmol g⁻¹ h⁻¹). In addition, we investigated the impact of Pt cocatalyst loading by photodeposition of 1.5 wt% of Pt onto the nanoparticles, which unexpectedly resulted in a reduced HER rate of 125 mmol g⁻¹ h⁻¹ (Figure 5a; Figure S45, Supporting Information). This trend was further confirmed using PF_gBT_{SO}-T₅₀ dispersions, where Pt deposition similarly led to a decrease in the HER rates (Figure S45, Supporting Information). Notably, the addition of the Pt cocatalyst did not induce any observable changes in the nanoparticle absorption profile, particle size, or photoluminescence spectra (Figure S46, Supporting Information).

To further investigate the effect of Pt loading on other conjugated materials, two polar polymers PF_gBT and P(Qx8O-T) with benzothiadiazole (BT) and quinoxaline (QX) units,^[62] respectively, were selected and processed as aqueous dispersions using nanoprecipitation technique (Figure 5b; Figures S47 and S48, Supporting Information). Upon photocatalytic experiments without Pt cocatalyst, low HER rates were achieved for PF_gBT (1.2 mmol g⁻¹ h⁻¹) and P(Qx8O-T) (0.6 mmol g⁻¹ h⁻¹) dispersions (Figure 5c). However, the addition of 1.5wt% of Pt resulted in an enhancement of their HER rates up to 5.4 and 2.3 mmol g⁻¹ h⁻¹, respectively, corresponding to a 4-fold enhancement in photocatalytic activity. This trend contrasts with the behaviour of PF_gBT_{SO}-T₂₅, where the introduction of Pt led to reduced performance, further supporting the existence of distinct hydrogen evolution mechanisms in BT_{SO}-based materials (Figure S49, Supporting Information). Notably, the presence of metallic cocatalyst resulted in quenched emissions in the case of PF_gBT and P(Qx8O-T) nanoparticles, attesting efficient charge transfer from polymer to metallic cocatalyst, while no quenching but an enhanced emission was observed in the case of PF_gBT_{SO}-T₂₅ nanoparticles (Figure S50, Supporting Information). These observations indicate that cocatalyst content alone (whether Pd or Pt) cannot universally account for the hydrogen evolution efficiency in BT_{SO}-containing systems, as schematized in Figure 5d.

Since the presence of cocatalyst does not directly correlate with high HER rates, a second hypothesis to explore is that the sulfone group is responsible for the reduction of protons to hydrogen gas. Under this assumption, photocatalytic efficiency would be predominantly governed by the number of BT_{SO} units incorporated in the polymer. The PF_gBT_{SO}-T_x series (ranging from PF_gBT_{SO} to PF_gBT_{SO}-T₇₅) provides an ideal platform to examine this possibility. We investigated all key features that could explain the differences in HER rates, and a more detailed discussion is provided in Note S3 (Supporting Information). A comparable residual content of Pd was measured for all PF_gBT_{SO}-T_x polymers (Table S9, Supporting Information), and no clear correlation between Pd content and HER rates could be identified. In addition, no correlation could be made regarding the evolution of LUMO levels and nanoparticle size for PF_gBT_{SO}-T_x polymers. However, strong correlations were observed between HER rates and other factors, including absorption onset, excited-state lifetimes, and the number of sulfone units.

Among the series, PF_gBT_{SO}-T₂₅—containing 25% thiophene units—displayed an optimal combination of these features, aligning with its superior HER performance (Figure S51,

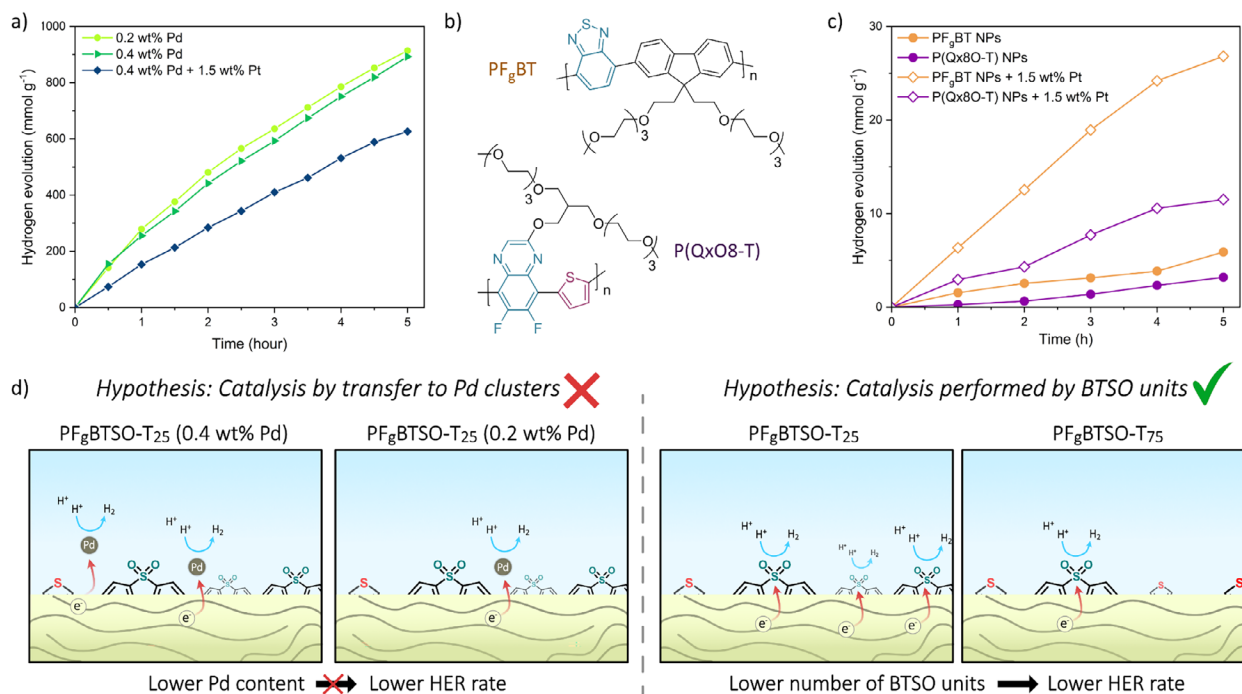


Figure 5. a) Hydrogen evolution of PF_g BT SO-T₂₅ NPs with different Pd loadings and with Pt-cocatalyst photodeposited in situ, in presence of 0.1 m of AA (using top-irradiation setup). b) Chemical structure of PF_g BT and P(Qx8O-T) polymers used for Pt-free photocatalysis. Accepting units are highlighted in blue and donating in red. c) HER rates of PF_g BT and P(Qx8O-T) dispersions, with and without Pt cocatalyst and in presence of 0.1 m of AA. d) Schematic illustration of hypotheses to explain the hydrogen production from BT SO-based polymers: catalysed only by a transfer of Pd cluster (left) and catalysis performed by the BT SO units (right).

Supporting Information). In contrast, PF_g BT SO-T₅₀, despite having a higher loading of Pd (0.4wt%), more redshifted absorption and most long-lived excited state (>1 ns), showed a significantly lower HER rate than PF_g BT SO-T₂₅ comprising lower residual Pd but a higher content of BT SO units. While the role of Pd in proton reduction cannot be entirely dismissed, it is unlikely to be the dominant factor influencing the photocatalytic behaviour of PF_g BT SO-T_x materials. Importantly, achieving state-of-the-art HER rates using low-cost, Pt-free systems highlights the promising potential of BT SO-based materials for sustainable photocatalysis.

To further isolate the role of the sulfone group, we assessed hydrogen evolution using the monomeric units BT SO and BT, thus eliminating any influence of Pd contamination introduced during polymerization. Both monomers displayed absorption profiles limited in the UV region (Figure S52a, Supporting Information), restricting their light-harvesting capabilities. Nevertheless, upon photocatalysis in the presence of AA, only the BT SO monomer displayed detectable hydrogen evolution, while no hydrogen could be quantified for the BT unit (Figure S52b, Supporting Information). Future work will focus on elucidating the underlying mechanism and on designing sulfone-functionalized systems with enhanced efficiency and stability for metal-free photocatalysis.

3. Conclusion

In this work we demonstrated the design of a simple conjugated polymer capable of efficient photocatalytic hydrogen evolution

without the use of a Pt cocatalyst. Once assembled as nanoparticles through the nanoprecipitation technique, state-of-the-art HER performance can be achieved without the need for a Pt cocatalyst, highlighting its potential as a cost-effective and scalable alternative for photocatalytic hydrogen production.

The selection of a polar accepting unit, such as BT SO, enabled an excellent interaction between the polymer backbone and the aqueous medium, while acting as the active site for proton reduction. The introduction of polar OEG side chains instead of alkyl ones proved to be crucial for hydrogen generation, achieving an almost 30-fold improvement in HER rates (3 to 90 mmol g⁻¹ h⁻¹). The origin of this improvement was mostly linked to more hydrated structure, which allowed better accessibility for redox species to the polymer backbone. In addition, a change in nanoparticle morphology upon introduction of ionic species appeared to be the key behind extended excited-state lifetime, beneficial for providing charges more time to be involved in hydrogen photocatalysis. The introduction of a D-A structure with addition of thiophene units resulted in improved absorption range and excited state lifetime. Optimum HER efficiencies were achieved for polymers with low thiophene content (< 25%), highlighting the balance between optoelectronic properties and the number of BT SO units.

An exceptional HER rate of 209 mmol g⁻¹ h⁻¹ (157 μmol h⁻¹) was achieved without Pt-cocatalyst, outperforming not only Pt-free aqueous dispersions, but also most of Pt-containing aqueous dispersions reported in the literature. We also highlighted that the pH, often overlooked, can significantly affect the efficiencies, with an optimum pH value of 2.5 to reach a balance between

available protons and deprotonated form of ascorbic acid, necessary for hole transfer. However, it is important to note that sacrificial electron donors like ascorbic acid and triethylamine can themselves contribute to hydrogen generation and should be considered carefully when evaluating photocatalyst efficiency.^[63]

Based on our findings, we propose five key design principles for future development of efficient, Pt-free organic photocatalysts: (i) accepting units should have a high polarity to ensure close interaction with reactive species in addition to promote interaction with redox species; (ii) polar side chains can promote the formation of hydrated nanoparticles and allow excellent water permeation; (iii) nanoparticle formation should aim toward highly porous structures and consider upscalability; (iv) the nanoparticle size must be controlled to ensure both stability and large specific surface; (v) absorption should be targeting visible/NIR range to maximize the number of available photons while ensuring a better photostability.

This work challenges the paradigm that organic materials require either the use of noble metal cocatalyst or two-component systems to achieve high hydrogen evolution production. By simplifying material design and eliminating costly cocatalysts, we demonstrate a viable path toward scalable, low-cost, and high-performance photocatalytic systems. These findings lay the foundation for a new generation of metal-free organic photocatalysts capable of addressing global energy and sustainability challenges.

Supporting Information

Supporting Information is available from the Wiley Online Library or from the author.

Acknowledgements

The authors acknowledge the Swedish Research Council (2020-05223), the Swedish Research Council Formas (2023-01008), the Swedish Energy Agency (P2021-90067), and the Wallenberg Foundation (2022.0192) for financial support. We thank the Swedish Research Council (2020-05223) and STandUP for Energy collaboration for financial support. Computations were performed at NSC Tetralith provided by the National Academic Infrastructure for Supercomputing in Sweden (NAISS) funded by the Swedish Research Council through grant agreement no. 2022-06725 (NAISS). RRB acknowledges also financial support from CAPES-PRINT exchange grant (88887.937407/2024-00) and São Paulo Research Foundation (FAPESP-2022/04379-3).

Conflict of Interest

The authors declare no conflict of interest.

Author Contributions

A.H. and J.P. contributed equally to this work. E.W. conceived the idea and supervised the project together with J. Z. A.H. and L.W. synthesized and characterized the materials. A.H. and J.P. prepared aqueous dispersions and performed the photocatalytic tests. L.F., R.R.B. and C.M.A. performed theoretical investigations comprising DFT calculations and molecular dynamics. A.H., J.P. and L.F. wrote the original draft. All authors were involved in the reviewing and editing of the manuscript.

Data Availability Statement

The data that support the findings of this study are available from the corresponding author upon reasonable request.

Keywords

aqueous dispersions, conjugated polymer, dibenzothiophene sulfone, hydrogen photocatalysis, Pt-free

Received: April 23, 2025

Revised: June 3, 2025

Published online: July 22, 2025

- [1] M. Ball, M. Weeda, *Int. J. Hydrogen Energy* **2015**, *40*, 7903.
- [2] K. Maeda, *ACS Catal.* **2013**, *3*, 1486.
- [3] B. A. Pinaud, J. D. Benck, L. C. Seitz, A. J. Forman, Z. Chen, T. G. Deutsch, B. D. James, K. N. Baum, G. N. Baum, S. Ardo, H. Wang, E. Miller, T. F. Jaramillo, *Energy Environ. Sci.* **2013**, *6*, 1983.
- [4] *Handbook of Conducting Polymers, Fourth Edition - 2 Volume Set*, 0 ed., (Eds.: J. R. Reynolds, B. C. Thompson, T. A. Skotheim), CRC Press, Florida, USA, **2019**.
- [5] Z. Genene, W. Mammo, E. Wang, M. R. Andersson, *Adv. Mater.* **2019**, *31*, 1807275.
- [6] C. M. Aitchison, I. McCulloch, *Chem. Mater.* **2024**, *36*, 1781.
- [7] C. Dai, S. Xu, W. Liu, X. Gong, M. Panahandeh-Fard, Z. Liu, D. Zhang, C. Xue, K. Ping Loh, B. Liu, *Small* **2018**, *14*, 1801839.
- [8] C. Han, S. Xiang, S. Jin, L.-W. Luo, C. Zhang, C. Yan, J.-X. Jiang, *J. Mater. Chem. A* **2022**, *10*, 5255.
- [9] R. J. Lyons, Y. Yang, E. McQueen, L. Luo, A. I. Cooper, M. A. Zwijnenburg, R. S. Sprick, *Adv. Energy Mater.* **2024**, *14*, 2303680.
- [10] S. A. J. Hillman, R. S. Sprick, D. Pearce, D. J. Woods, W.-Y. Sit, X. Shi, A. I. Cooper, J. R. Durrant, J. Nelson, *J. Am. Chem. Soc.* **2022**, *144*, 19382.
- [11] M. Sachs, R. S. Sprick, D. Pearce, S. A. J. Hillman, A. Monti, A. A. Y. Guilbert, N. J. Brownbill, S. Dimitrov, X. Shi, F. Blanc, M. A. Zwijnenburg, J. Nelson, J. R. Durrant, A. I. Cooper, *Nat. Commun.* **2018**, *9*, 4968.
- [12] S. Jin, C. Han, S. Xiang, C. Zhang, J.-X. Jiang, *J. Catal.* **2023**, *427*, 115091.
- [13] Z.-R. Tan, Y.-Q. Xing, J.-Z. Cheng, G. Zhang, Z.-Q. Shen, Y.-J. Zhang, G. Liao, L. Chen, S.-Y. Liu, *Chem. Sci.* **2022**, *13*, 1725.
- [14] Y. Liu, J. Wu, F. Wang, S. Dibenzothiophene-S, *Appl. Catal., B* **2022**, *307*, 121144.
- [15] Z. Li, F. Zhao, Y. Chu, F. Meng, Y. Dong, H. Zhang, J. Zhao, Y. Du, S. Wang, *ACS Sustainable Chem. Eng.* **2024**, *12*, 1072.
- [16] W. Lin, Y. Wu, Y. Sun, M. M. Elsenety, W. Lin, J. Yen, H. Hsu, B. Chen, H. Huang, C. Chang, T. Huang, Y. Zhuang, Y. Tseng, K. Lin, S. Yang, C. Yu, H. Chou, *Angew Chem Int Ed* **2024**, *63*, 202407702.
- [17] A. Holmes, E. Deniau, C. Lartigau-Dagron, A. Bousquet, S. Chambon, N. P. Holmes, *ACS Nano* **2021**, *15*, 3927.
- [18] M. Yu, W. Zhang, Z. Guo, Y. Wu, W. Zhu, *Angew Chem Int Ed* **2021**, *60*, 15590.
- [19] J. Kosco, M. Bidwell, H. Cha, T. Martin, C. T. Howells, M. Sachs, D. H. Anjum, S. Gonzalez Lopez, L. Zou, A. Wadsworth, W. Zhang, L. Zhang, J. Tellam, R. Sougrat, F. Laquai, D. M. DeLongchamp, J. R. Durrant, I. McCulloch, *Nat. Mater.* **2020**, *19*, 559.
- [20] J. Kosco, S. Gonzalez-Carrero, C. T. Howells, T. Fei, Y. Dong, R. Sougrat, G. T. Harrison, Y. Firdaus, R. Sheelamanthula, B. Purushothaman, F. Moruzzi, W. Xu, L. Zhao, A. Basu, S. De Wolf, T. D. Anthopoulos, J. R. Durrant, I. McCulloch, *Nat. Energy* **2022**, *7*, 340.

- [21] A. Dolan, J. M. De La Perrelle, T. D. Small, E. R. Milsom, G. F. Metha, X. Pan, M. R. Andersson, D. M. Huang, *ACS Appl. Nano Mater.* **2022**, 5, 12154.
- [22] N. P. Holmes, S. Chambon, A. Holmes, X. Xu, K. Hirakawa, E. Deniau, C. Lartigau-Dagron, A. Bousquet, *Curr. Opin. Colloid Interface Sci.* **2021**, 56, 101511.
- [23] M. V. Pavliuk, S. Wrede, A. Liu, A. Brnovic, S. Wang, M. Axelsson, H. Tian, *Chem. Soc. Rev.* **2022**, 51, 6909.
- [24] Y. Zhu, Z. Zhang, W. Si, Q. Sun, G. Cai, Y. Li, Y. Jia, X. Lu, W. Xu, S. Zhang, Y. Lin, *J. Am. Chem. Soc.* **2022**, 144, 12747.
- [25] M. H. Elsayed, M. Abdellah, A. Z. Alhakemy, I. M. A. Mekhemer, A. E. A. Aboubakr, B.-H. Chen, A. Sabbah, K.-H. Lin, W.-S. Chiu, S.-J. Lin, C.-Y. Chu, C.-H. Lu, S.-D. Yang, M. G. Mohamed, S.-W. Kuo, C.-H. Hung, L.-C. Chen, K.-H. Chen, H.-H. Chou, *Nat. Commun.* **2024**, 15, 707.
- [26] Y. Yang, D. Li, J. Cai, H. Wang, C. Guo, S. Wen, W. Li, T. Wang, D. Liu, *Adv Funct Materials* **2023**, 33, 2209643.
- [27] Y. Liang, T. Li, Y. Lee, Z. Zhang, Y. Li, W. Si, Z. Liu, C. Zhang, Y. Qiao, S. Bai, Y. Lin, *Angew Chem Int Ed* **2023**, 62, 202217989.
- [28] Y. Feng, S. Gong, Y. Wang, C. Ban, X. Qu, J. Ma, Y. Duan, C. Lin, D. Yu, L. Xia, X. Chen, X. Tao, L. Gan, X. Zhou, *Adv. Mater.* **2025**, 37, 2412965.
- [29] Y. Shi, L. Li, Z. Xu, X. Qin, Y. Cai, W. Zhang, W. Shi, X. Du, F. Guo, *J. Colloid Interface Sci.* **2023**, 630, 274.
- [30] Y. Hu, Y. Liu, J. Wu, Y. Li, J. Jiang, F. Wang, *ACS Appl. Mater. Interfaces* **2021**, 13, 42753.
- [31] G. Shu, Y. Li, Z. Wang, J.-X. Jiang, F. Wang, *Appl. Catal., B* **2020**, 261, 118230.
- [32] M. Axelsson, Z. Xia, S. Wang, M. Cheng, H. Tian, *JACS Au* **2024**, 4, 570.
- [33] L. Wang, R. Fernández-Terán, L. Zhang, D. L. A. Fernandes, L. Tian, H. Chen, H. Tian, *Angew Chem Int Ed* **2016**, 55, 12306.
- [34] A. Liu, C.-W. Tai, K. Holá, H. Tian, *J. Mater. Chem. A* **2019**, 7, 4797.
- [35] J. Kosco, I. McCulloch, *ACS Energy Lett.* **2018**, 3, 2846.
- [36] E. Wang, L. Hou, Z. Wang, S. Hellström, F. Zhang, O. Inganäs, M. R. Andersson, *Adv. Mater.* **2010**, 22, 5240.
- [37] J. J. Rech, J. Neu, Y. Qin, S. Samson, J. Shanahan, R. F. Josey, H. Ade, W. You, *ChemSusChem* **2021**, 14, 3561.
- [38] C. M. Aitchison, R. S. Sprick, A. I. Cooper, *J. Mater. Chem. A* **2019**, 7, 2490.
- [39] L. Parrenin, C. Brochon, G. Hadziioannou, E. Cloutet, *Macromol. Rapid Commun.* **2015**, 36, 1816.
- [40] Y. Wang, T. Yokota, T. Someya, *NPG Asia Mater* **2021**, 13, 22.
- [41] X. Lin, Y. Liang, Z. Hu, X. Zhang, Y. Liang, Z. Hu, F. Huang, Y. Cao, *Nanomaterials* **2022**, 12, 1535.
- [42] K. Fischer, P. Marlow, F. Manger, C. Sprau, A. Microfluidics Colsmann, *Adv Materials Technologies* **2022**, 7, 2200297.
- [43] R. Couto, S. Chambon, C. Aymonier, E. Mignard, B. Pavageau, A. Erriguible, S. Marre, *Chem. Commun.* **2015**, 51, 1008.
- [44] G. Bonfante, F. Awai, T. Kubo, H. Segawa, S. H. Kim, A. Genot, S. Chambon, *Materials Today Sustainability* **2024**, 27, 100920.
- [45] A. Holmes, H. Laval, M. Schmutz, S. Blanc, J. Allouche, B. Watts, G. Wantz, N. P. Holmes, K. Hirakawa, E. Deniau, S. Chambon, C. Lartigau-Dagron, A. Bousquet, *Mater. Today Chem* **2022**, 26, 101229.
- [46] Y.-J. Tu, D. Njus, H. B. Schlegel, *Org. Biomol. Chem.* **2017**, 15, 4417.
- [47] L. R. Franco, P. Park, H. Chaimovich, K. Coutinho, I. M. Cuccovia, F. S. Lima, *RSC Adv.* **2022**, 12, 4573.
- [48] Z. Hu, Z. Wang, X. Zhang, H. Tang, X. Liu, F. Huang, Y. Cao, *iScience* **2019**, 13, 33.
- [49] J. Kosco, S. Gonzalez-Carrero, C. T. Howells, W. Zhang, M. Moser, R. Sheelamanthula, L. Zhao, B. Willner, T. C. Hidalgo, H. Faber, B. Purushothaman, M. Sachs, H. Cha, R. Sougrat, T. D. Anthopoulos, S. Inal, J. R. Durrant, I. McCulloch, *Adv. Mater.* **2022**, 34, 2105007.
- [50] J. Brebels, J. V. Manca, L. Lutsen, D. Vanderzande, W. Maes, *J. Mater. Chem. A* **2017**, 5, 24037.
- [51] R. Sakai, *Polym J* **2016**, 48, 59.
- [52] H. Liu, X. Hao, C. Duan, H. Yang, Y. Lv, H. Xu, H. Wang, F. Huang, D. Xiao, Z. Tian, *Nanoscale* **2013**, 5, 9340.
- [53] T. Eder, T. Stangl, M. Gmelch, K. Remmerssen, D. Laux, S. Höger, J. M. Lupton, J. Vogelsang, *Nat. Commun.* **2017**, 8, 1641.
- [54] A. Brnovic, L. Hammarström, H. Tian, *J. Phys. Chem. C* **2023**, 127, 12631.
- [55] D. J. Woods, S. A. J. Hillman, D. Pearce, L. Wilbraham, L. Q. Flagg, W. Duffy, I. McCulloch, J. R. Durrant, A. A. Y. Guilbert, M. A. Zwijnenburg, R. S. Sprick, J. Nelson, A. I. Cooper, *Energy Environ. Sci.* **2020**, 13, 1843.
- [56] W.-C. Lin, J. Jayakumar, C.-L. Chang, L.-Y. Ting, M. H. Elsayed, M. Abdellah, K. Zheng, A. M. Elewa, Y.-T. Lin, J.-J. Liu, W.-S. Wang, C.-Y. Lu, H.-H. Chou, *Appl. Catal., B* **2021**, 298, 120577.
- [57] A. Liu, S. Wang, H. Song, Y. Liu, L. Gedda, K. Edwards, L. Hammarström, H. Tian, *Phys. Chem. Chem. Phys.* **2023**, 25, 2935.
- [58] S. An, Z. Wu, H. Jeong, J. Lee, S. Y. Jeong, W. Lee, S. Kim, J. W. Han, J. Lim, H. Cha, H. Y. Woo, D. S. Chung, *Small* **2023**, 19, 2204905.
- [59] M. V. Pavliuk, S. Wrede, H. Tian, *Chem. Commun.* **2023**, 59, 5611.
- [60] Y. Bai, L. Wilbraham, H. Gao, R. Clowes, H. Yang, M. A. Zwijnenburg, A. I. Cooper, R. S. Sprick, *J. Mater. Chem. A* **2021**, 9, 19958.
- [61] M. Sachs, H. Cha, J. Kosco, C. M. Aitchison, L. Francàs, S. Corby, C.-L. Chiang, A. A. Wilson, R. Godin, A. Fahey-Williams, A. I. Cooper, R. S. Sprick, I. McCulloch, J. R. Durrant, *J. Am. Chem. Soc.* **2020**, 142, 14574.
- [62] T. T. Filate, S. Lee, L. R. Franco, Q. Chen, Z. Genene, C. F. N. Marchiori, Y. Lee, M. Araujo, W. Mammo, H. Y. Woo, B. J. Kim, E. Wang, *ACS Appl. Mater. Interfaces* **2024**, 16, 12886.
- [63] F. Costantino, P. V. Do Kamat, *ACS Energy Lett.* **2022**, 7, 242.